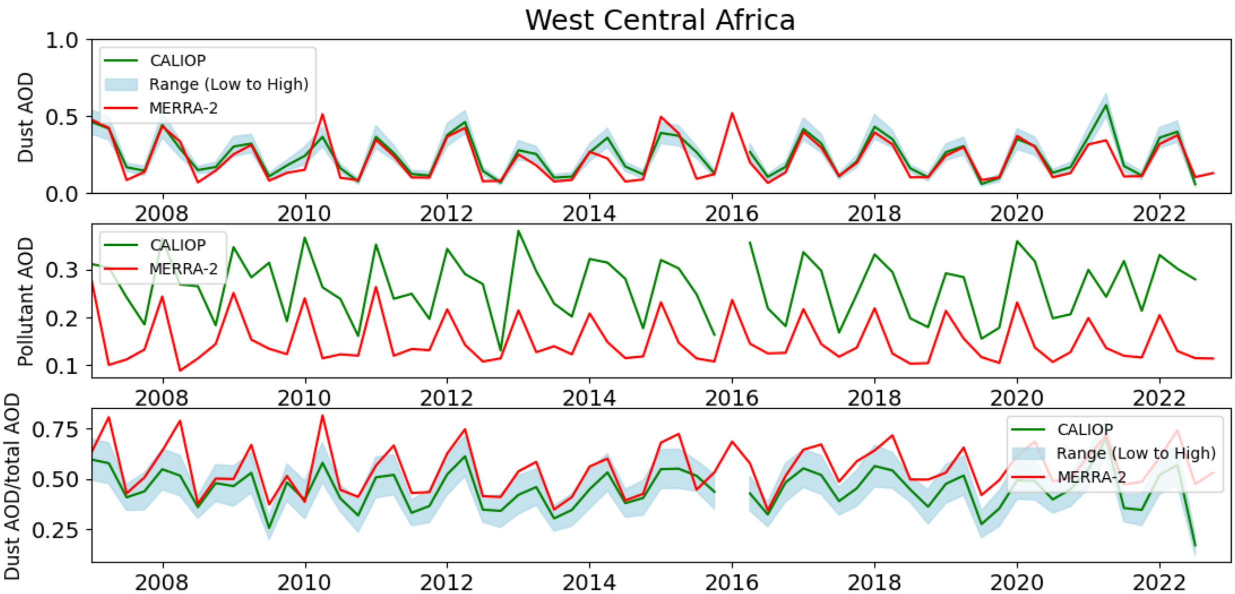

Figure S1. Time series of seasonal-mean aerosol optical depth (AOD) over West Central Africa (6°N–9°N, 15°W–0°W) from 2007 to 2022. (a) Dust AOD derived from CALIOP DAOD (green) with the low–high uncertainty range (light-blue shading), compared with dust AOD from MERRA-2 (red). (b) Non-dust (pollution) AOD, defined as total DAOD minus dust DAOD, from CALIOP (green) and MERRA-2 (red). (c) Fraction of dust in the total DAOD (dust/DAOD) from CALIOP (green, with uncertainty range in light blue) and from MERRA-2 (red).

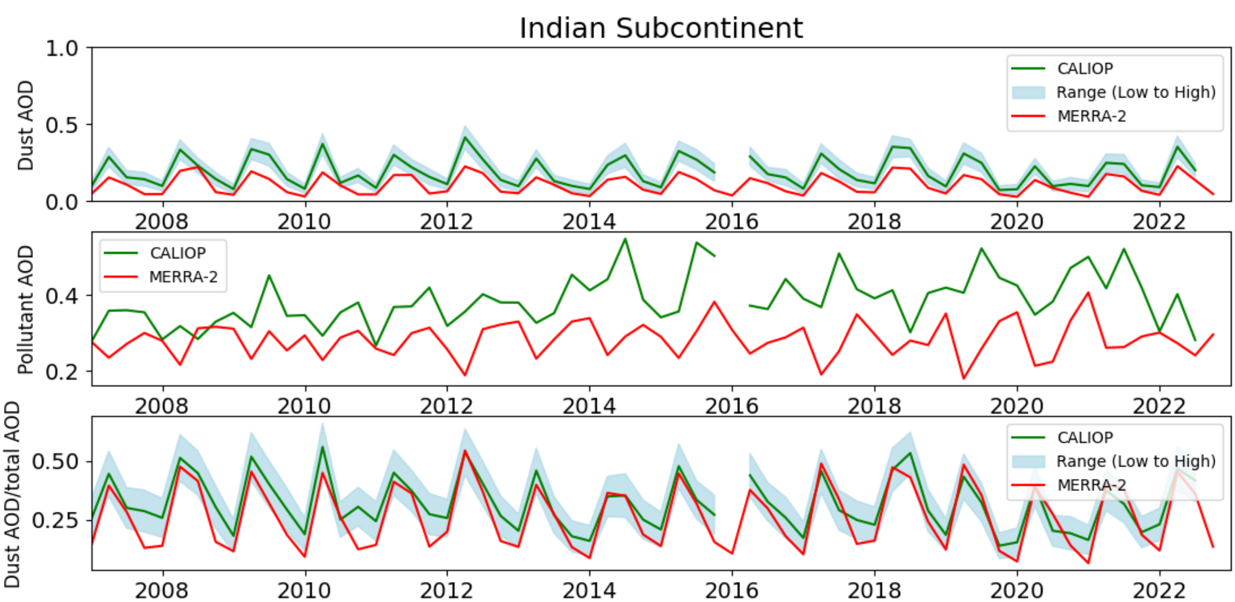

Figure S2. Same as Figure S1, but for the Indian Subcontinent (18°N–26°N, 70°E–85°E).

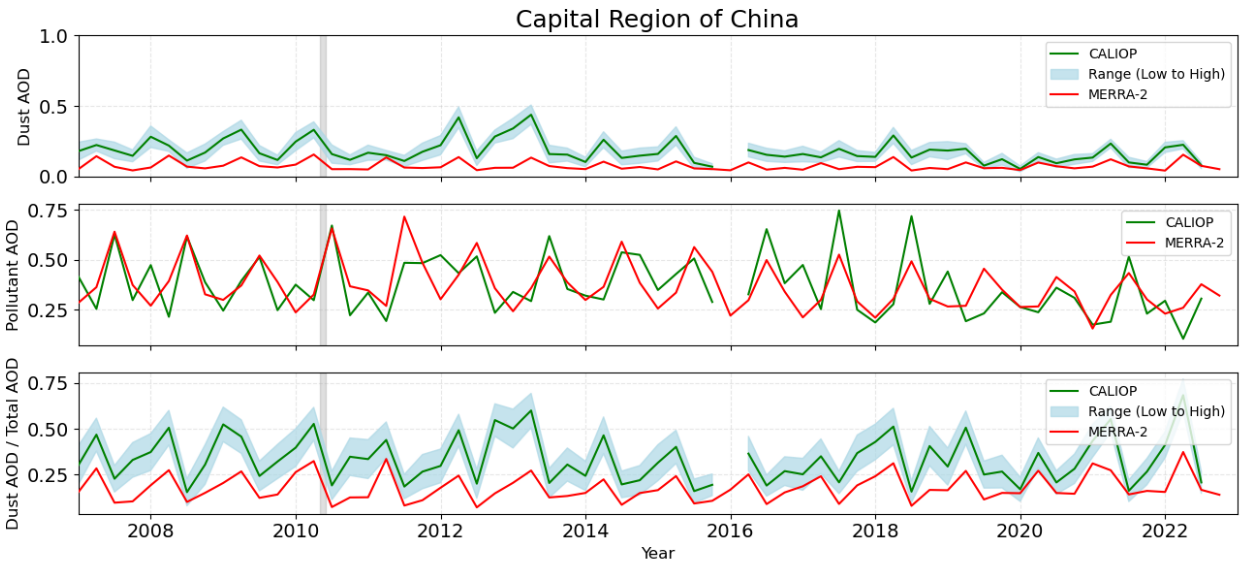

Figure S3. Same as Figure S1, but for the Capital Region of China (36°N–40°N, 110°E–117°E). The gray shading denotes the May 2010 case analyzed for the Capital Region of China in Sect. 4.

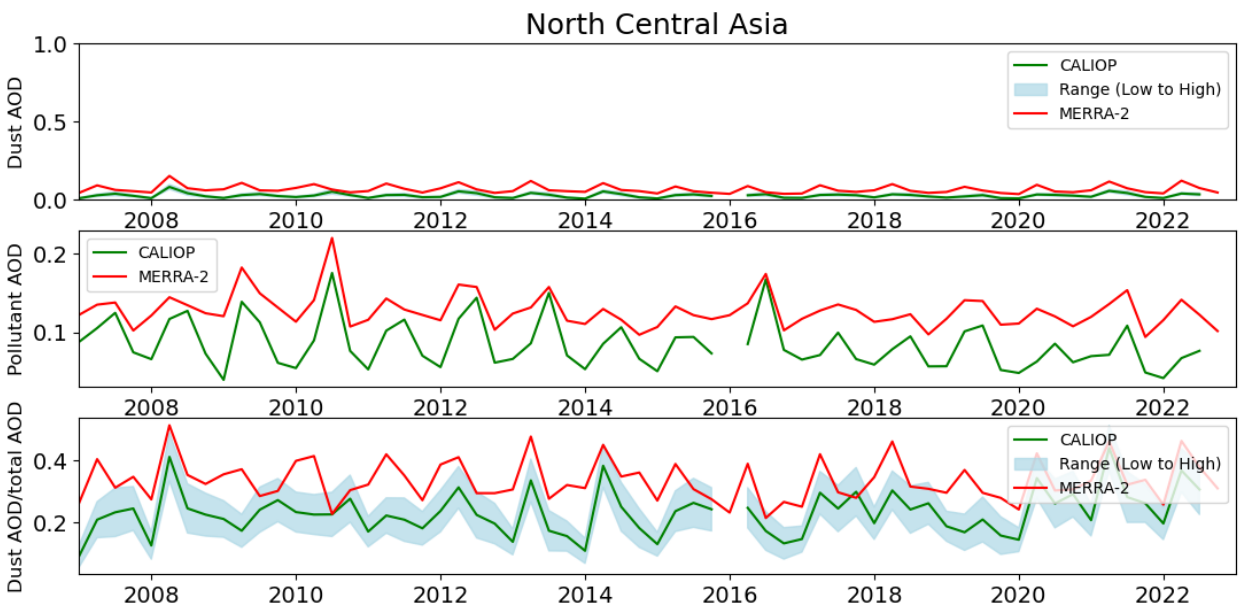

Figure S4. Same as Figure S1, but for the northern Central Asia (45°N–52°N, 35°E–65°E).

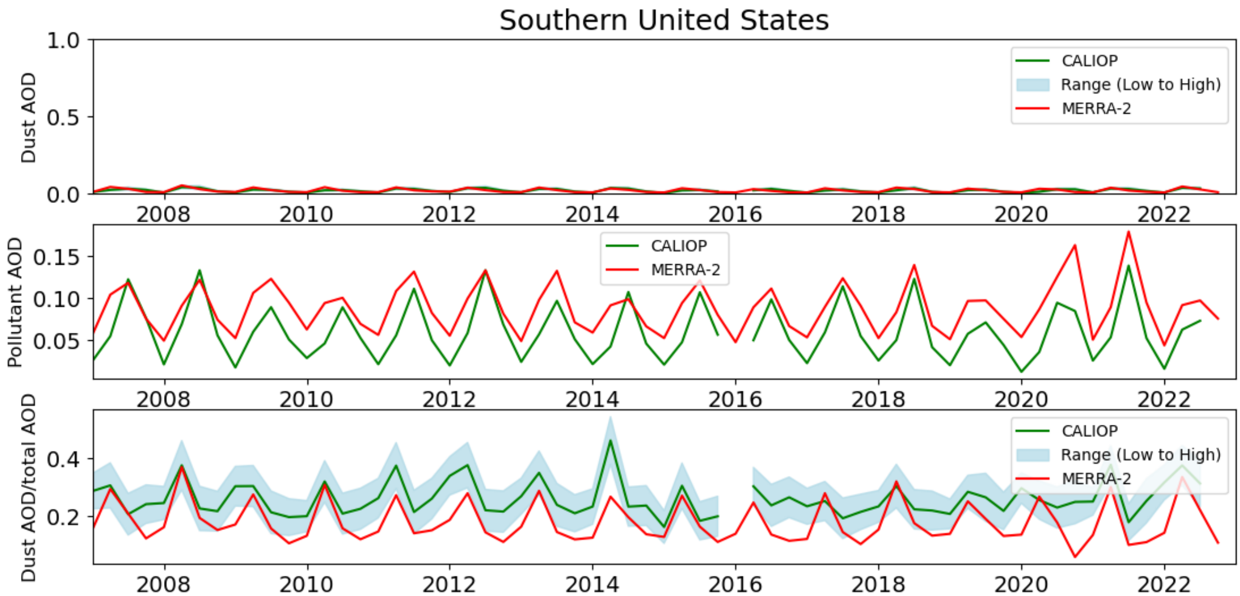

Figure S5. Same as Figure S1, but for the southern United States (30°N–40°N, 120°W–95°W).

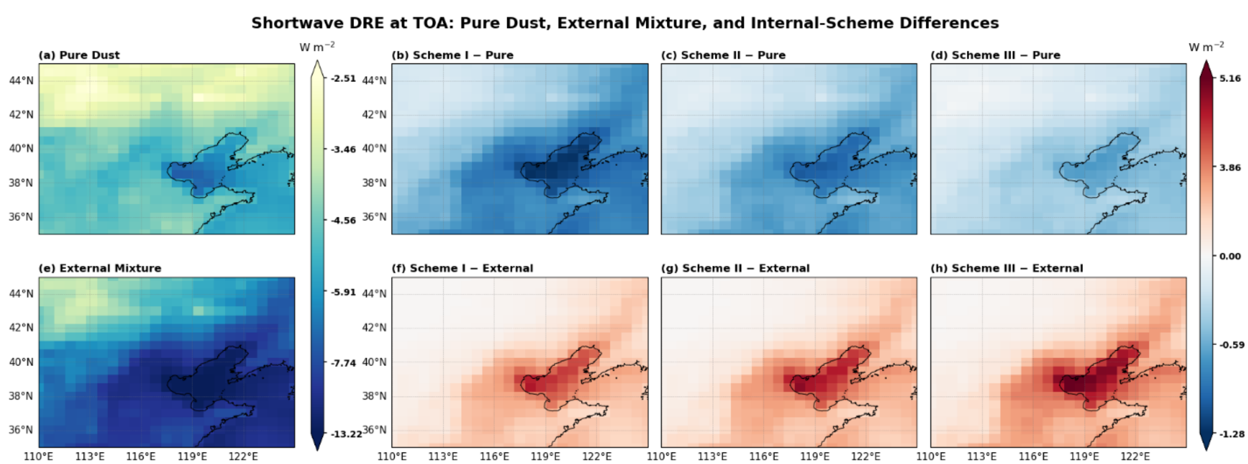

Figure S6. Shortwave dust DRE at TOA over the Capital Region of China in May 2010, computed with the Rapid Radiative Transfer Model (RRTM) under four dust–sulfate mixing assumptions. Panels (a) and (e) show the DRE of pure dust and of the fully externally mixed polluted dust, respectively, which serve as references. Panels (b)–(d) show the DRE differences of internally mixed Schemes I–III relative to pure dust, and panels (f)–(h) show the corresponding differences relative to the external mixture.

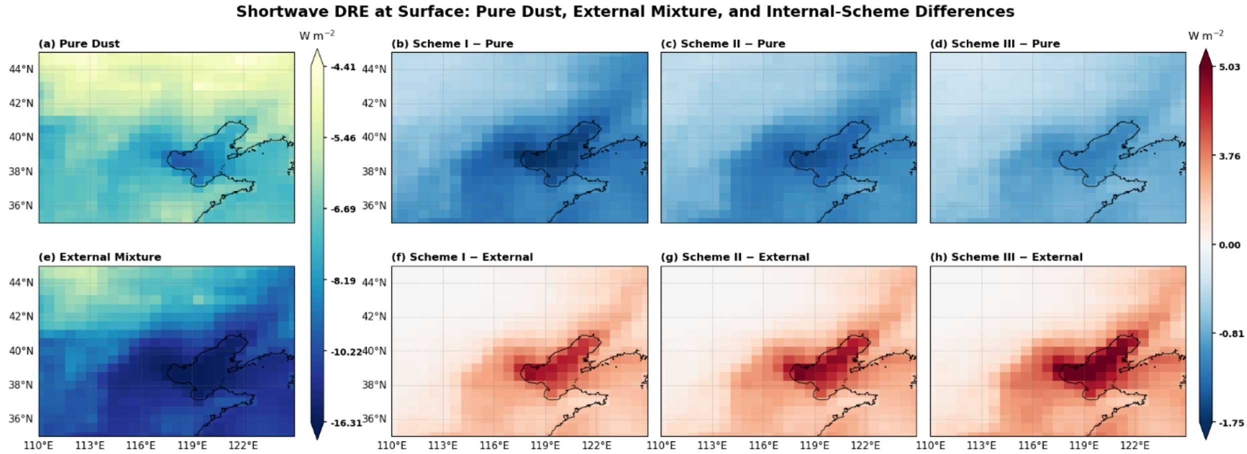

Figure S7. Shortwave dust DRE at the surface over the Capital Region of China in May 2010, computed with the Rapid Radiative Transfer Model (RRTM) under four dust–sulfate mixing assumptions. Panels (a) and (e) show the DRE of pure dust and of the fully externally mixed polluted dust, respectively, which serve as references. Panels (b)–(d) show the DRE differences of internally mixed Schemes I–III relative to pure dust, and panels (f)–(h) show the corresponding differences relative to the external mixture.

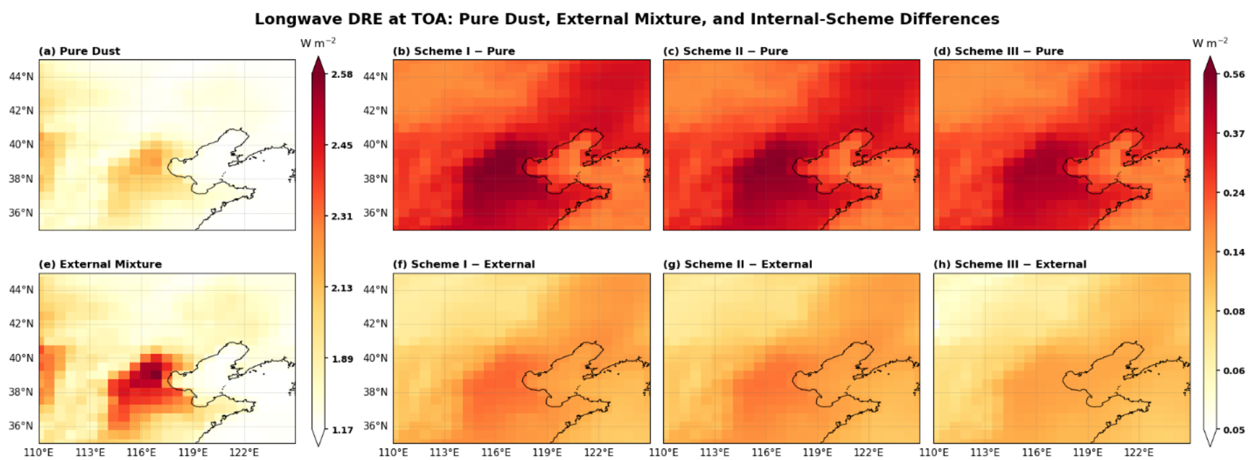

Figure S8. Longwave dust DRE at TOA over the Capital Region of China in May 2010, computed with the Rapid Radiative Transfer Model (RRTM) under four dust–sulfate mixing assumptions. Panels (a) and (e) show the DRE of pure dust and of the fully externally mixed polluted dust, respectively, which serve as references. Panels (b)–(d) show the DRE differences of internally mixed Schemes I–III relative to pure dust, and panels (f)–(h) show the corresponding differences relative to the external mixture.

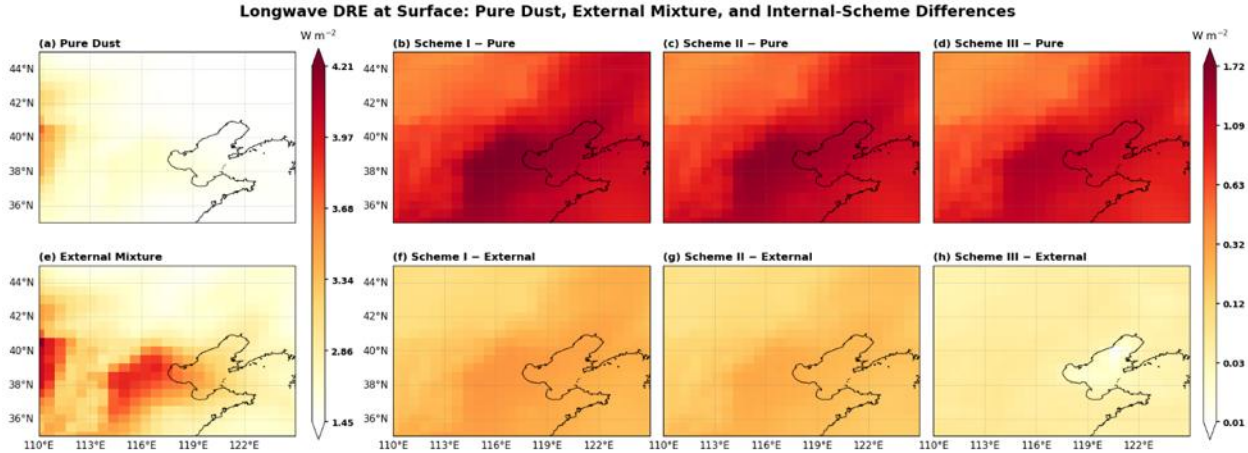

Figure S9. Longwave dust DRE at the surface over the Capital Region of China in May 2010, computed with the Rapid Radiative Transfer Model (RRTM) under four dust–sulfate mixing assumptions. Panels (a) and (e) show the DRE of pure dust and of the fully externally mixed polluted dust, respectively, which serve as references. Panels (b)–(d) show the DRE differences of internally mixed Schemes I–III relative to pure dust, and panels (f)–(h) show the corresponding differences relative to the external mixture.

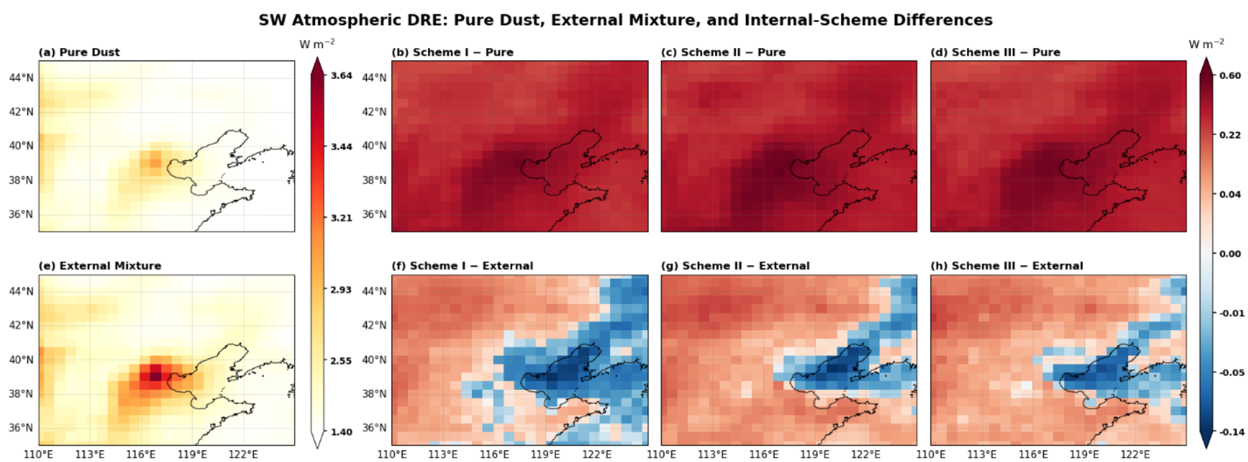

Figure S10. Shortwave atmospheric dust DRE, defined as the TOA DRE minus the surface DRE, over the Capital Region of China in May 2010, computed with the Rapid Radiative Transfer Model (RRTM) under four dust–sulfate mixing assumptions. Panels (a) and (e) show the DRE of pure dust and of the fully externally mixed polluted dust, respectively, which serve as references. Panels (b)–(d) show the DRE differences of internally mixed Schemes I–III relative to pure dust, and panels (f)–(h) show the corresponding differences relative to the external mixture.

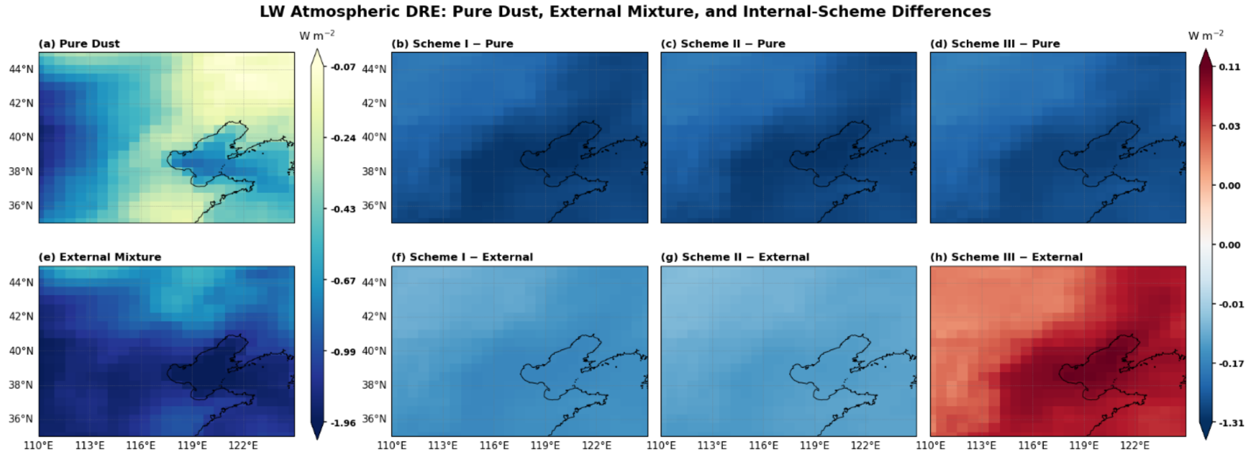

Figure S11. Longwave atmospheric dust DRE, defined as the TOA DRE minus the surface DRE, over the Capital Region of China in May 2010, computed with the Rapid Radiative Transfer Model (RRTM) under four dust–sulfate mixing assumptions. Panels (a) and (e) show the DRE of pure dust and of the fully externally mixed polluted dust, respectively, which serve as references. Panels (b)–(d) show the DRE differences of internally mixed Schemes I–III relative to pure dust, and panels (f)–(h) show the corresponding differences relative to the external mixture.

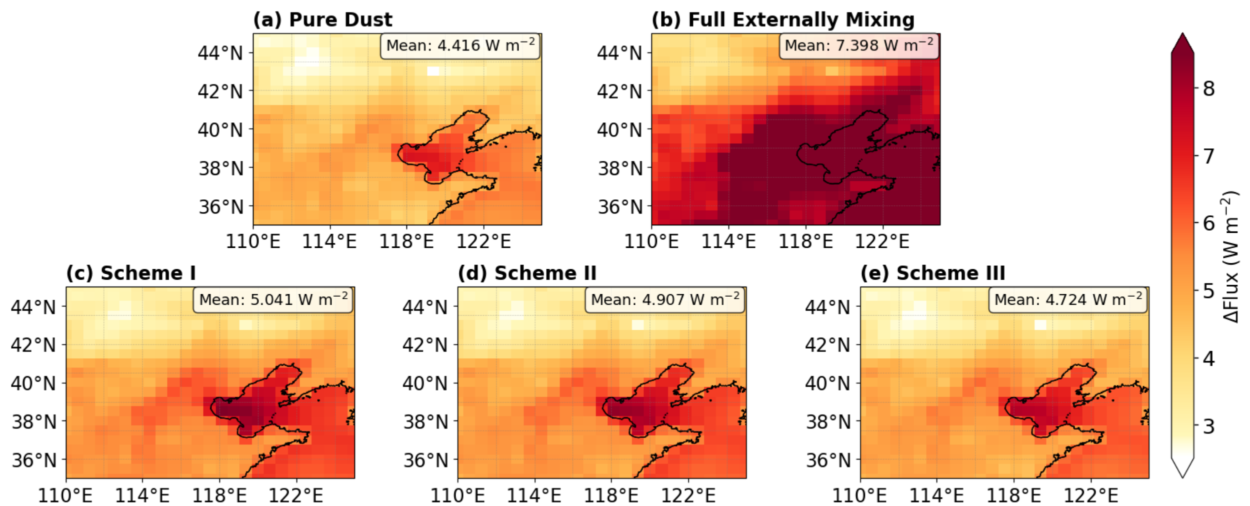

Figure S12. Change in TOA upward shortwave flux (aerosol − clean sky) over the Capital Region of China in May 2010 for different aerosol mixing conditions. Panels (a)–(e) correspond to pure dust, full external mixing, and internal mixing schemes I–III, respectively. Shading shows the TOA upward flux perturbation $\Delta F_{\uparrow}$ in $W \cdot m^{-2}$, and the regional mean $\Delta F_{\uparrow}$ is annotated in each panel.

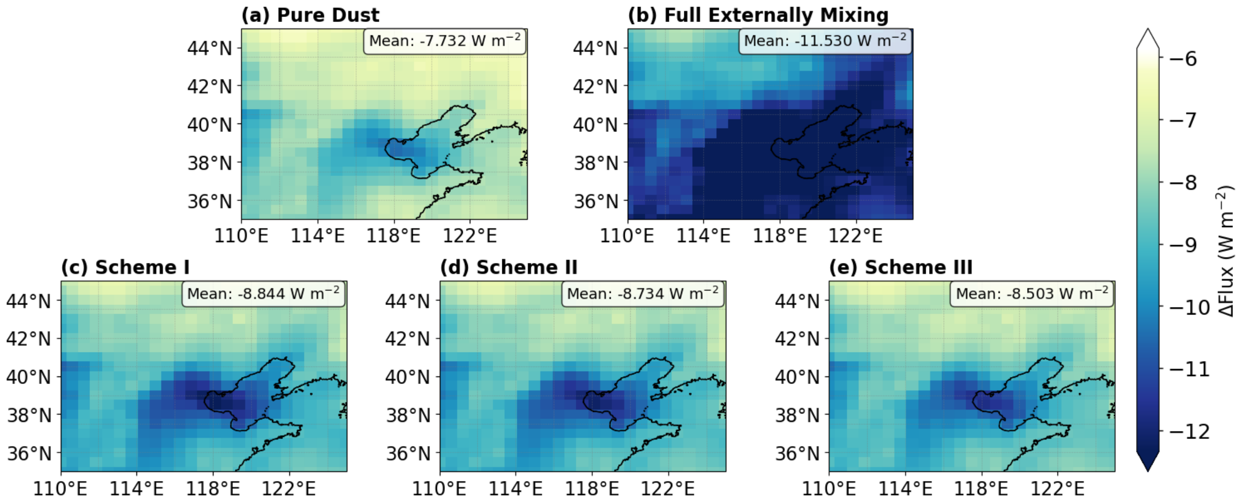

Figure S13. Change in surface downward shortwave flux (aerosol − clean sky) over the Capital Region of China in May 2010 for different aerosol mixing conditions. Panels (a)–(e) correspond to pure dust, full external mixing, and internal mixing schemes I–III, respectively. Shading shows the surface downward flux perturbation $\Delta F_{\downarrow}$ in W·m^{-2}, and the regional mean $\Delta F_{\downarrow}$ is annotated in each panel.

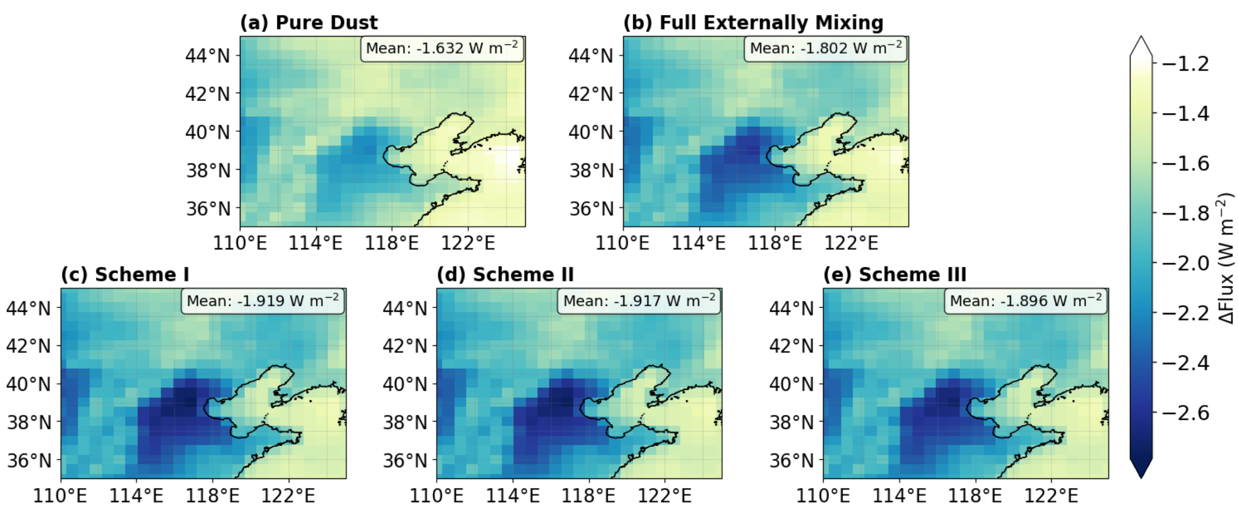

Figure S14. Same as Figure S12, but for TOA upward longwave flux difference (aerosol − clean-sky) over the Capital Region of China.

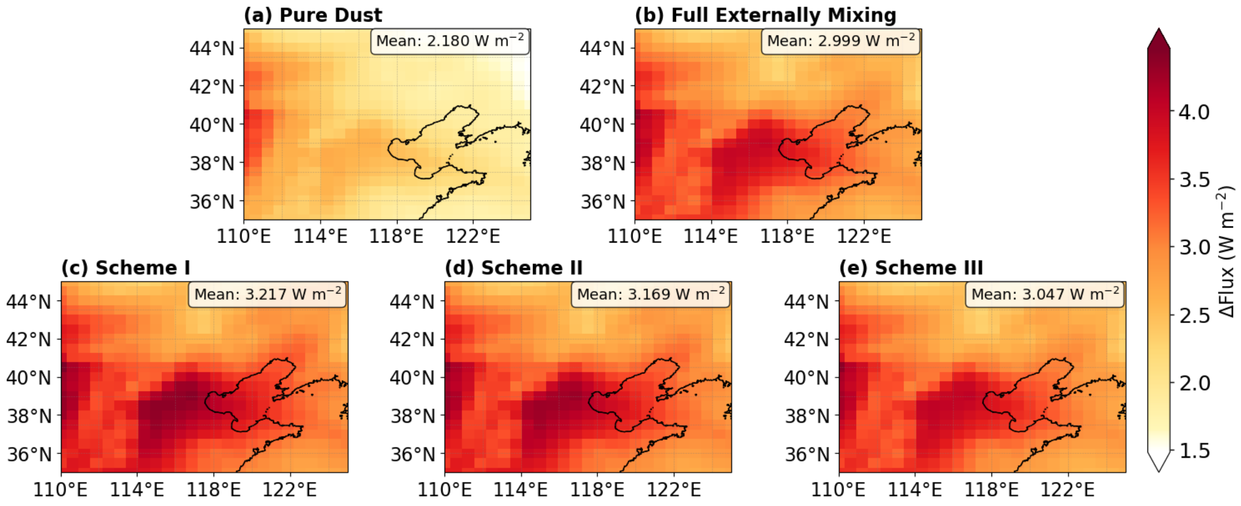

745 **Figure S15.** Same as Figure S12, but for surface downward longwave flux difference (aerosol − clean-sky) over the Capital Region of China.